Orbital Many-Body Dynamics of Bosons in the Second Bloch Band of an Optical Lattice

J. Vargas,[1] M. Nuske,[1,2,3] R. Eichberger,[1,2] C. Hippler,[1] L. Mathey,[1,2,3] and A. Hemmerich[1,2,3]
[1]*Institut für Laserphysik, Universität Hamburg, 22761 Hamburg, Germany*
[2]*Zentrum für Optische Quantentechnologien, Universität Hamburg, 22761 Hamburg, Germany*
[3]*The Hamburg Center for Ultrafast Imaging, Luruper Chaussee 149, Hamburg 22761, Germany*

(Received 12 August 2020; accepted 27 April 2021; published 17 May 2021)

We explore Josephson-like dynamics of a Bose-Einstein condensate of rubidium atoms in the second Bloch band of an optical square lattice providing a double well structure with two inequivalent, degenerate energy minima. This oscillation is a direct signature of the orbital changing collisions predicted to arise in this system in addition to the conventional on-site collisions. The observed oscillation frequency scales with the relative strength of these collisional interactions, which can be readily tuned via a distortion of the unit cell. The observations are compared to a quantum model of two single-particle modes and to a semiclassical multiband tight-binding simulation of 12×12 tubular sites of the lattice. Both models reproduce the observed oscillatory dynamics and show the correct dependence of the oscillation frequency on the ratio between the strengths of the on-site and orbital changing collision processes.

DOI: 10.1103/PhysRevLett.126.200402

The ground state wave function of bosonic atoms in optical lattices [1–5] can be generally chosen to be real and positive [6–8], giving rise to a rather featureless physical scenario, in contrast to electronic condensed-matter lattice physics, where a more complex structure such as orbital degrees of freedom of higher bands typically provides a richer physical reality, for example in the case of transition metal oxides [9,10]. In contrast to the well-controlled and comparatively simple platform of optical lattices, in electronic condensed-matter examples, however, the discrimination of physics related to orbital degrees of freedom from the multitude of other possible mechanisms is difficult. This has triggered growing interest to study atoms in metastable higher Bloch bands of optical lattice potentials [7,8,11–21]. The presence of energetically degenerate orbitals with different angular momenta and orientations gives rise to multiple degenerate global band minima in the single-particle band structure at different high-symmetry points within the first Brillouin zone. This results in the intriguing consequence that even tiny energy scales as that of weak contact interactions play a decisive role in determining the structure of the lowest-energy state in each band. The presence of degenerate local orbitals enables contact interaction processes, which change the orbital character of the colliding atoms [8,12,22]. Such processes have been identified as essential for the experimentally observed formation of multiorbital Bose-Einstein condensates (BEC) with interaction-induced local angular momentum [8,12,16,18]. Theoretical proposals have also pointed out the possibility of global angular momentum [23,24]. While equilibrium phases have been studied in some detail, the study of nonequilibrium scenarios has remained limited to one-dimensional examples [25,26].

In this work, we experimentally and theoretically explore quantum dynamics reminiscent of Josephson oscillations of bosonic atoms in the second band of an optical lattice, which provides a double well structure in quasimomentum space with two inequivalent energy minima. These oscillations are driven by the interplay between orbital changing collisions and conventional on-site collisions. Their relative strength, which can be readily tuned via a distortion of the unit cell, determines the oscillation frequency. Note that orbital changing collisions show some analogy to spin changing collisions [27]. Our work is the first to extend the experimental study of interaction dynamics in optical lattices with bosons from the familiar lowest band examples to orbital optical lattices, which possess higher order orbitals. The future perspective of this work is to trigger further research aiming at a better understanding of the nature of contact interaction in the presence of orbital degrees of freedom, including processes as the spontaneous generation of local or global angular momentum [8].

We selectively populate one of the two degenerate global energy minima in the second Bloch band of an optical square lattice with a BEC and observe the subsequent dynamics, which displays a damped oscillation of population between both energy minima. This oscillation is exclusively driven by two kinds of collisional interactions, i.e., the on-site collisions of atoms in either of the three local orbitals s, p_x, and p_y, respectively, and an orbital changing collision mimicking a pair tunneling process [22,28,29], where two atoms colliding, e.g., in the p_x orbital at some lattice site, are both transferred to the p_y orbital or vice versa. According to our model calculations, the frequency of the population oscillation scales with the relative strength of these collisional interactions, which can

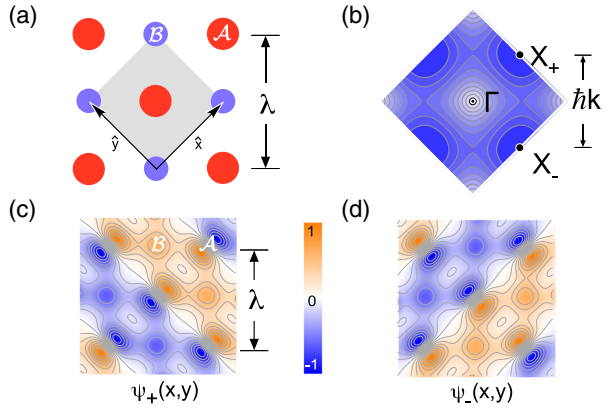

FIG. 1. (a) The bipartite lattice geometry with deep $\mathcal{A}$ sites and shallow $\mathcal{B}$ sites. The unit cell is shown by the gray rectangle. (b) The second Bloch band of the lattice in (a) is plotted across the first Brillouin zone with the two inequivalent energy minima at $X_\pm$ and the energy maximum at Γ highlighted. Blue denotes low and white denotes high energy. (c) and (d) show contour plots of the Bloch functions $\psi_\pm$, corresponding to the $X_\pm$ points of the second band.

be readily tuned in the experiment. We implement two different models both describing essential aspects of our experimental findings: a quantum two-mode model involving the two Bloch modes associated with the energy minima of the second band, and a simulation of 12×12 tubular sites according to Fig. 1(a), treated in a four-band tight-binding approach accounting for nearest- and next-nearest-neighbor tunneling and on-site contact interactions.

We consider a two-dimensional (2D) optical square lattice in the xy plane, composed of deep and shallow wells arranged according to the black and white fields of a checkerboard, see Fig. 1(a). In the third dimension, i.e., the z direction, a nearly harmonic potential with $\Omega/2\pi \approx 40$ Hz is applied, such that the 3D lattice potential constitutes a 2D lattice of elongated sites. The 2D lattice potential is well approximated by $V(x,y) \approx -V_0|\cos(kx) + e^{i\theta}\cos(ky)|^2$ with $k = 2\pi/\lambda$ and $\lambda = 1064$ nm. Adjustment of θ permits controlled rapid tuning of the potential energy difference $\Delta V \equiv -4V_0\cos(\theta)$ between $\mathcal{A}$ and $\mathcal{B}$ wells. Technical details are given in Ref. [19]. In its second Bloch band this lattice provides two inequivalent degenerate local energy minima at the high-symmetry points X_+ and X_-, located at the edge of the first Brillouin zone, see Fig. 1(b). The corresponding Bloch functions, ψ_+ and ψ_-, composed of p orbitals in the deep $\mathcal{A}$ wells and s orbitals in the shallow $\mathcal{B}$ wells, are orthogonal real-valued standing waves [cf. Figs. 1(c) and 1(d)].

We prepare the initial state with the following protocol. A nearly pure rubidium BEC with up to 6×10^4 atoms in the $|F = 2, m_F = 2\rangle$ hyperfine state at about 50 nK temperature is initially loaded at the Γ point in the lowest band of the lattice potential with $\Delta V_i = -1.23V_{0,i}$ and $V_{0,i} = 4.3E_{\mathrm{rec}}$. Here, $E_{\mathrm{rec}} \equiv \hbar^2k^2/(2m)$ denotes the single-photon recoil energy and m is the atomic mass. At this stage, the negative sign of ΔV_i indicates that the $\mathcal{B}$ wells are deep and the $\mathcal{A}$ wells are shallow. The atoms reside nearly exclusively in the $\mathcal{B}$ wells. Next, a magnetic field gradient realizes a magnetic force. The gradient is applied for 0.65 ms, such that the atoms undergo a half-cycle of a Bloch oscillation, and hence are transferred to the X_+ point. Details of this step are deferred to Ref. [30]. Finally, ΔV and V_0 are ramped up in 0.3 ms to final values $\Delta V_f \in [0.55, 0.75] \times V_{0,f}$ and $V_{0,f} = 7.2E_{\mathrm{rec}}$. According to the positive value of ΔV_f the roles of $\mathcal{A}$ and $\mathcal{B}$ wells are swapped such that a condensate at the X_+ point in the second band is formed with 25.000 ± 2.000 atoms [19,30]. Subsequently, the temporal evolution of the relative population difference between the X_- and the X_+-point $(n_- - n_+)/(n_- + n_+)$ is recorded. This quantity is retrieved by performing band mapping or alternatively, by recording momentum spectra, and counting the atoms in the vicinity of the $X_\pm$ points. Details are found in Ref. [30]. An example for $\Delta V_f = 0.725 \times V_{0,f}$ is shown in Fig. 2(a). A strongly damped oscillation is observed at a frequency of 21.6 Hz. Corresponding band mapping pictures recorded at times indicated by dashed gray lines are shown on the upper edge of Fig. 2(a). The red solid line is a fit with a single exponentially damped harmonic oscillation. In Fig. 2(b), for each data point the procedure to obtain Fig. 2(a) is repeated and the observed oscillation frequencies ν_{osc} are plotted versus ΔV_f. The plot shows an increase of ν_{osc} with increasing ΔV_f.

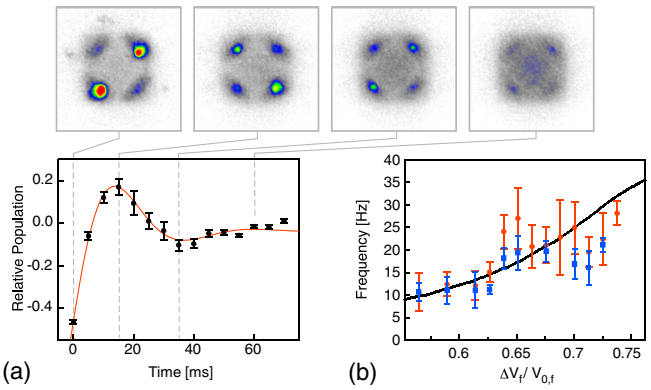

FIG. 2. (a) The temporal evolution of the relative population difference $(n_- - n_+)/(n_- + n_+)$ is shown for fixed $\Delta V_f = 0.725 \times V_{0,f}$ after initially a BEC is formed at the X_+ point. The red solid line is a fit by an exponentially damped harmonic oscillation. The error bars show the standard deviations of the mean for a set of ten measurements. (b) The observed oscillation frequencies obtained from fitting data as in (a) are plotted versus ΔV_f. The errors show the standard deviations found in the fits. The red disks and the blue squares represent two measurement series evaluated via momentum spectra and band mapping, respectively. The solid black line shows a calculation using a two-mode model.

In the following, we will compare the data points in Fig. 2(b) with two distinct models, which will both allow us to directly connect the experimental parameter ΔV_f with the amplitude ratio between an orbital interaction process exchanging pairs of atoms between p_x and p_y orbitals and conventional Hubbard-like on-site interaction. We begin with a minimal model of the two Bloch modes ψ_+ and ψ_-. According to Ref. [22], the Hamiltonian reads

$$H = \frac{g_0}{2}[\hat{n}_+(\hat{n}_+ - 1) + \hat{n}_-(\hat{n}_- - 1)] + \frac{g_1}{2}[4\hat{n}_+\hat{n}_- + \hat{\psi}_+^\dagger\hat{\psi}_+^\dagger\hat{\psi}_-\hat{\psi}_- + \hat{\psi}_-^\dagger\hat{\psi}_-^\dagger\hat{\psi}_+\hat{\psi}_+], \quad (1)$$

with $\hat{\psi}_\pm$ denoting the annihilation operator for the Bloch modes $\psi_\pm$ and $\hat{n}_\pm \equiv \hat{\psi}_\pm^\dagger\hat{\psi}_\pm$ the corresponding number operators. As seen in Eq. (1), g_0 corresponds to a conventional Hubbard on-site interaction, while the expression controlled by g_1 contains a pair exchange term between both modes, which changes the orbital flavor. As detailed in Ref. [30], the collision parameters g_0 and g_1 can be expressed as $g_0 = g_{2D}I_0(\Delta V_f)$ and $g_1 = g_{2D}I_1(\Delta V_f)$ with an effective 2D collision energy g_{2D} and the dimensionless integrals $I_0(\Delta V_f) \equiv A\int_A dxdy|\tilde{\psi}_\pm|^4$ and $I_1(\Delta V_f) \equiv A\int_A dxdy|\tilde{\psi}_+|^2|\tilde{\psi}_-|^2$, where $\tilde{\psi}_\pm$ denote the Bloch wave functions normalized to a single unit cell of the lattice with area $A = \lambda^2/2$. In order to model the observation in Fig. 2(b), the following steps are performed. A numerical band calculation is performed to obtain $\tilde{\psi}_\pm$ and hence the integrals $I_0(\Delta V_f)$ and $I_1(\Delta V_f)$ as functions of ΔV_f. The effective collision parameter g_{2D} is expressed in terms of the 3D collision parameter for rubidium atoms (cf. Ref. [30]). The Schrödinger equation for the Hamiltonian of Eq. (1) is solved for $N = 5.000$ particles, with the initial condition that all atoms reside at X_+. This leads to the full time evolution of the system state $|\Psi(t)\rangle$. Finally, the expectation value $\langle\Psi(t)|(\hat{n}_+ - \hat{n}_-)|\Psi(t)\rangle/N$ is obtained, a fast Fourier transform of this quantity is calculated and the frequency ν_{osc} of the dominant spectral component is determined. To estimate the prediction for $N = 24.000$ particles (which results in a good match with the observations), we calculate ν_{osc} as a function of N, for the range of $N = 20$ to $N = 500$. The resulting dependence of ν_{osc} on N is described by a power-law of the form $\sim N^{0.8896}$, within a relative error of 10^{-4}. Utilizing this dependence, we extrapolate the value of ν_{osc} calculated for $N = 5.000$ to find that for $N = 24.000$ (cf. [33]). The resulting ν_{osc} plotted against ΔV_f is shown as the black solid line in Fig. 2(b). A detailed treatment of the underlying two-mode model is found in Ref. [22]. Remarkably, the observed ascending trend of ν_{osc} is well reproduced by the model although band relaxation, heating, and particle loss are neglected here. The band calculation of $I_0(\Delta V_f)$ and $I_1(\Delta V_f)$ shows that within the accessible range $\Delta V_f \in [0.2, 0.73] \times V_{0,f}$, increasing ΔV_f acts to increase the quantity $g_2 \equiv 1 - g_1/g_0$. The two-mode model [22] predicts self-trapping (cf. Ref. [34]) to occur if $g_2 > 2/3$, which, however, corresponds to values of ΔV_f well outside of this range, such that the band structure would no longer support a stable BEC in the second band.

In order to obtain a more realistic description including dissipation and loss, we turn to a model consisting of 12×12 tubular sites according to Fig. 1(a) treated in a tight-binding approach accounting for nearest-neighbor and next-nearest-neighbor tunneling and the same on-site collisions already included in the model in Eq. (1). The tubes are mapped onto a 1D lattice by discretizing them in real space with a discretization length of 0.13 μm. We simulate the experimental loading protocol and the subsequent dynamics using classical-field-theory techniques, see Ref. [30]. We initialize the c-field propagation from a thermal ensemble of temperature T using Monte Carlo sampling with parameters $V_{0,i} = 4.3E_{rec}$ and $\Delta V_i = -1.23V_{0,i}$. We transfer the atoms to the X_+ point using phase imprinting, see Ref. [30], and quench the potential offset to its final value $\Delta V_f \in [0.2, 0.73] \times V_{0,f}$ with $V_{0,f} = 7.2E_{rec}$. The resulting time evolution of the relative population of the X points is shown in Fig. 3(a). For a single initialization and a temperature $k_BT = 0.8E_{rec}$, similar to what is realized experimentally, we observe coherent oscillations between the X_+ and X_- points during the first hundred milliseconds before damping by decay to the lower band sets in. In Ref. [30] we show that at lower temperatures, band relaxation and decay of the condensate fractions become negligible, and hence, for single initializations, coherent oscillations prevail for very long times. However, the frequency and phase of these oscillations vary for different initializations, which leads to additional strong damping via decoherence, when averaging over multiple

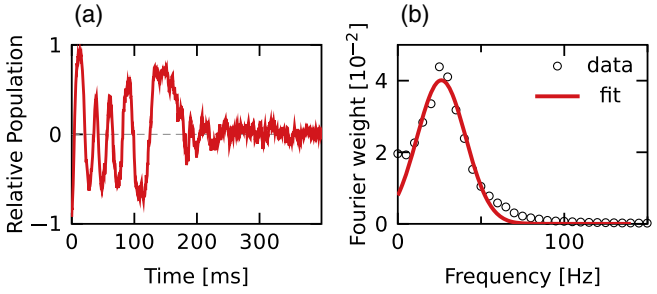

FIG. 3. (a) Relative population difference of X points $(n_- - n_+)/(n_- + n_+)$ according to our classical-field-theory simulations at $\Delta V_f = 0.69V_0$. The panel shows the oscillation for a single random initialization. (b) Fourier spectrum of the oscillation shown in (a) averaged over 500 random initializations, see black circles. The peak of the Fourier transform determines the main oscillation frequency at the given value of ΔV_f. The red line shows a Gaussian fit to the Fourier spectrum. For details on the fitting routine see Ref. [30]. For both panels the temperature is $T = 76.8$ nK $\approx 0.8E_{rec}/k_B$ and hence similar to the experimental temperature.

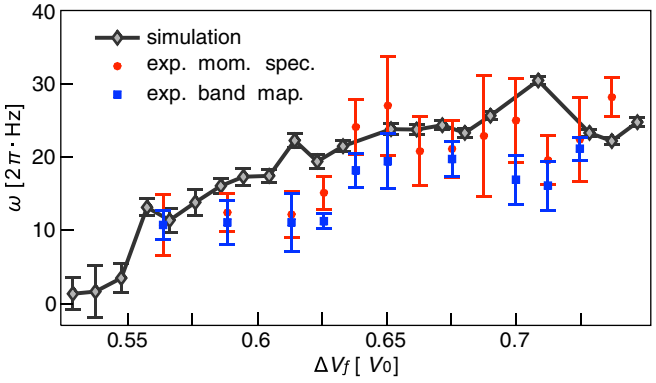

FIG. 4. Dominant oscillation frequencies obtained from c-field simulations, see black diamonds, are compared to experimental data, shown by blue squares and red disks, which are repeated from Fig. 2(b). For each ΔV_f we determine the averaged Fourier spectrum, as exemplarily shown in Fig. 3(b) and plot the dominant frequency obtained from a Gaussian fit. The errors in the determination of the positions of the maxima of the fitted Gaussians are mostly smaller than the data symbols.

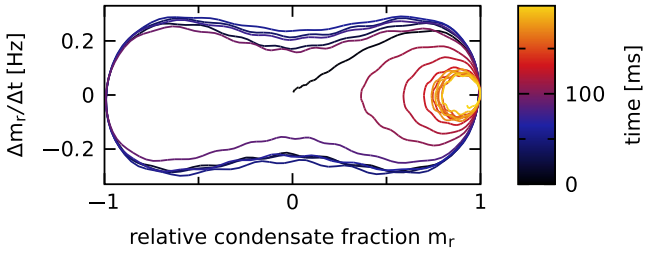

FIG. 5. Phase-space diagram of the relative population in the two lowest-energy many-body states m_r for a single initialization of our simulations. Here, $m_r = m_+(t) - m_-(t)$ and $m_\pm(t) = |\langle\Psi_\pm|\psi(t)\rangle|^2/m_0$. Furthermore $\psi(t)$ is the wave function obtained within our simulations and $m_0 = |\langle\Psi_+|\psi(t)\rangle|^2 + |\langle\Psi_-|\psi(t)\rangle|^2$ is the total number of condensed atoms in the second band. We consider an idealized case at lower temperature $T = 0.5$ nK and 4 times stronger interactions as compared to Fig. 4. We also use a different quench protocol that keeps $V_0 = 7E_{\mathrm{rec}}$ throughout the quench and changes ΔV from $\Delta V_i = -0.6V_0$ to $\Delta V_f = 0.35V_0$.

initializations is performed (see Ref. [30]). Recall that the experimental data in Fig. 2(a) correspond to an average over ten initializations. As illustrated by the error bars, the error for a single initialization increases during the first 30 ms, thus reflecting this expected decoherence. Only for later times, when atom loss in the second band sets in, the error bars decrease again. For our numerical simulations we estimate the dominant oscillation frequencies by calculating the power spectrum. We Fourier transform the relative population of the X points for each random initialization and subsequently average the Fourier spectra. The result is shown in Fig. 3(b). As expected, we find a broad Fourier peak, where many different oscillation frequencies contribute. We fit a Gaussian to the Fourier spectrum in order to extract the dominant oscillation frequency, for details see Ref. [30]. Figure 4 plots the results for different final potential offsets ΔV_f showing notable agreement with the experimental data repeated from Fig. 2(b).

Finally, we consider the equilibration dynamics after the quench within our c-field simulations. The two degenerate lowest-energy many-body states approximately form an N-fold occupation of either of the coherent superpositions $\Psi_\pm = \psi_+ \pm i\psi_-$ of the two degenerate single-particle states $\psi_\pm$ [12,16,19]. Their relative phases $\pm i$ minimize the energy associated with the pair exchange processes. We may consider the oscillatory dynamics that emerges in both experiment and simulations in terms of $\Psi_\pm$. To this end, we show in Fig. 5 the normalized projection of the state $\psi(t)$ onto $\Psi_\pm$. We consider an idealized only weakly damped case by choosing a low temperature of 0.5 nK. Initially, the atoms are prepared to occupy one of the X points and hence their overlap with both Ψ_+ and Ψ_- is 50%. Before damping sets in, the evolution is characterized by instanton-type dynamics [35], where the atoms perform perfect oscillations between $\Psi_\pm$. This reproduces the oscillations shown in Fig. 3(a) in the $\Psi_\pm$ basis, however at much lower temperature and hence lower damping. At the zero crossings in Fig. 3(a), the atoms have unit overlap with one of the two many-body states $\Psi_\pm$. A typical single-implementation trajectory plotted in Fig. 5 shows that this overlap alternates between Ψ_+ and Ψ_-, which amounts to an oscillating chirality. The slight inward shift of the trajectory at 50% mixture is a result of the slow-down due to the free-energy barrier that separates the two lowest-energy states $\Psi_\pm$. Eventually, due to damping, the atoms do not have enough energy to cross this barrier and spontaneously pick either of the two states $\Psi_\pm$. In the subsequent second part of the dynamics the atoms perform damped harmonic oscillations in the corresponding free-energy minimum and hence have an overlap between 50% and unity with this state. This example provides a limiting case of the many-dynamics of this system, for which the experimental results provide a more strongly damped realization.

In summary, we have studied quantum dynamics of a BEC in the second band of an optical lattice arising from the competition between orbital changing and conventional on-site collisions. A minimal quantum model and a more realistic model based on classical field simulations show quantitative agreement with the observations. For simulations of an idealized low-temperature scenario, we find coherent instanton-type dynamics characterized by oscillations between the two degenerate lowest-energy many-body states in the second band. Our work pioneers the exploration of quantum dynamics in optical lattices with orbital degrees of freedom and orbital degeneracies, which allows one to emulate a physical reality beyond s-band Hubbard physics.

We thank Max Hachmann for his contributions during the first stage of the experiment. We acknowledge partial support

from the Deutsche Forschungsgemeinschaft (DFG) through the collaborative research center SFB 925 (M. N. and L. M.), the Cluster of Excellence CUI: Advanced Imaging of Matter–EXC 2056–project ID 390715994 (M. N. and L. M.), and the individual grants program DFG-He2334/17-1 (A. H.). J. V. is grateful to the National Agency for Research and Development (ANID) of Chile and its Ph.D. scholarship program. M. N. acknowledges support from Stiftung der Deutschen Wirtschaft. We thank Juliette Simonet, Klaus Sengstock, and their entire team for useful discussions.

[1] P. Verkerk, B. Lounis, C. Salomon, C. Cohen-Tannoudji, J. Y. Courtois, and G. Grynberg, Phys. Rev. Lett. **68**, 3861 (1992).
[2] A. Hemmerich and T. W. Hänsch, Phys. Rev. Lett. **70**, 410 (1993).
[3] G. Grynberg and C. Robilliard, Phys. Rep. **355**, 335 (2001).
[4] I. Bloch, Nat. Phys. **1**, 23 (2005).
[5] M. Lewenstein *et al.*, Adv. Phys. **56**, 243 (2007).
[6] R. P. Feynman, *Statistical Mechanics: A Set of Lectures* (Addison-Wesley Publishing Company, Berlin, 1972).
[7] C. Wu, Mod. Phys. Lett. B **23**, 1 (2009).
[8] X. Li and W. V. Liu, Rep. Prog. Phys. **79**, 116401 (2016).
[9] Y. Tokura and N. Nagaosa, Science **288**, 462 (2000).
[10] S. Maekawa, T. Tohyama, S. E. Barnes, S. Ishihara, W. Koshibae, and G. Khaliullin, *Physics of Transition Metal Oxides*, Springer Series in Solid-State Sciences Vol. 144 (Springer, New York, 2004).
[11] A. Isacsson and S. M. Girvin, Phys. Rev. A **72**, 053604 (2005).
[12] W. V. Liu and C. Wu, Phys. Rev. A **74**, 013607 (2006).
[13] T. Müller, S. Fölling, A. Widera, and I. Bloch, Phys. Rev. Lett. **99**, 200405 (2007).
[14] J. Larson, A. Collin, and J.-P. Martikainen, Phys. Rev. A **79**, 033603 (2009).
[15] G. Wirth, M. Ölschläger, and A. Hemmerich, Nat. Phys. **7**, 147 (2011).
[16] M. Ölschläger, T. Kock, G. Wirth, A. Ewerbeck, C. Morais Smith, and A. Hemmerich, New J. Phys. **15**, 083041 (2013).
[17] X. Li, A. Paramekanti, A. Hemmerich, and W. V. Liu, Nat. Commun. **5**, 3205 (2014).
[18] T. Kock, M. Ölschläger, A. Ewerbeck, W.-M. Huang, L. Mathey, and A. Hemmerich, Phys. Rev. Lett. **114**, 115301 (2015).
[19] T. Kock, C. Hippler, A. Ewerbeck, and A. Hemmerich, J. Phys. B **49**, 042001 (2016).
[20] S. Jin, W. Zhang, X. Guo, X. Chen, X. Zhou, and X. Li, Phys. Rev. Lett. **126**, 035301 (2021).
[21] V. Sharma, S. Choudhury, and E. J. Mueller, Phys. Rev. A **101**, 033609 (2020).
[22] A. Hemmerich, Phys. Rev. A **99**, 013623 (2019).
[23] M. Di Liberto, A. Hemmerich, and C. Morais Smith, Phys. Rev. Lett. **117**, 163001 (2016).
[24] Z. F. Xu, L. You, A. Hemmerich, and W. V. Liu, Phys. Rev. Lett. **117**, 085301 (2016).
[25] Z. Wang, B. Yang, D. Hu, X. Chen, H. Xiong, B. Wu, and X. Zhou, Phys. Rev. A **94**, 033624 (2016).
[26] L. Niu, S. Jin, X. Chen, X. Li, and X. Zhou, Phys. Rev. Lett. **121**, 265301 (2018).
[27] A. Widera, F. Gerbier, S. Fölling, T. Gericke, O. Mandel, and I. Bloch, Phys. Rev. Lett. **95**, 190405 (2005).
[28] J.-Q. Liang, J.-L. Liu, W.-D. Li, and Z.-J. Li, Phys. Rev. A **79**, 033617 (2009).
[29] P. Bader and U. R. Fischer, Phys. Rev. Lett. **103**, 060402 (2009).
[30] See Supplemental Material at http://link.aps.org/supplemental/10.1103/PhysRevLett.126.200402 on the theoretical modeling, experimental procedures, and data analysis protocols, which includes Refs. [31,32].
[31] A. Hemmerich, D. Schropp, and T. W. Hänsch, Phys. Rev. A **44**, 1910 (1991).
[32] M. Nuske, J. Vargas, M. Hachmann, R. Eichberger, L. Mathey, and A. Hemmerich, Phys. Rev. Research **2**, 043210 (2020).
[33] In solving the two-mode model, the number of atoms N determines the dimension of the matrix to be diagonalized. Our numerical capacity has limited N to 5.000.
[34] M. Albiez, R. Gati, J. Fölling, S. Hunsmann, M. Cristiani, and M. K. Oberthaler, Phys. Rev. Lett. **95**, 010402 (2005).
[35] R. Rajaraman, Solitons and instantons, in *An Introduction to Solitons and Instantons in Quantum Field Theory* (North-Holland, Amsterdam, 1982).